International Journal of Minerals, Metallurgy and Materials
Volume 28, Number 12, December 2021, Page 2001
https://doi.org/10.1007/s12613-020-2229-3

Graphene oxide wrapped magnetic nanoparticle composites induced by SiO_2 coating with excellent regenerability

Zhong-liang Hu[1)], *Hou-quan Cui*[2)], *Yan-huai Ding*[3)], *Jing-ying Li*[1)], *Yi-rong Zhu*[1)], *and Zhao-hui Li*[2)]

1) College of Metallurgy and Material Engineering, Hunan University of Technology, Zhuzhou 412007, China
2) College of Chemistry, Xiangtan University, Xiangtan 411105, China
3) Institute of Fundamental Mechanics and Materials Engineering, Xiangtan University, Xiangtan 411105, China
(Received: 20 September 2020; revised: 19 November 2020; accepted: 20 November 2020)

Abstract: Graphene oxide (GO) wrapped Fe_3O_4 nanoparticles (NPs) were prepared by coating the Fe_3O_4 NPs with a SiO_2 layer, and then modifying by amino groups, which interact with the GO nanosheets to form covalent bonding. The SiO_2 coating layer plays a key role in integrating the magnetic nanoparticles with the GO nanosheets. The effect of the amount of SiO_2 on the morphology, structure, adsorption, and regenerability of the composites was studied in detail. An appropriate SiO_2 layer can effectively induce the GO nanosheets to completely wrap the Fe_3O_4 NPs, forming a core-shell Fe_3O_4@SiO_2@GO composite where Fe_3O_4@SiO_2 NPs are firmly encapsulated by GO nanosheets. The optimized Fe_3O_4@SiO_2@GO sample exhibits a high saturated adsorption capacity of 253 $mg \cdot g^{-1}$ Pb(II) cations from wastewater, and the adsorption process is well fitted by Langmuir adsorption model. Notably, the composite displays excellent regeneration, maintaining a ~90% adsorption capacity for five cycles, while other samples decrease their adsorption capacity rapidly. This work provides a theoretical guidance to improve the regeneration of the GO-based adsorbents.

Keywords: graphene oxide; ferroferric oxide; core-shell structure; adsorption; regeneration; covalent bonding; lead(II) removal

1. Introduction

Wastewater originating from industries, such as metallurgical, chemical manufacturing, and textile printing, contains many toxic pollutants that pose a great threat to our existence [1–2]. Many strategies have been proposed to remove the contaminants, including membrane filtration, ion exchange, and adsorption [3–6]. Among these methods, adsorption is very common because of its high efficiency, low cost, and environmental friendliness [7–8]. Traditional carbon materials, such as activated carbon, have been extensively used as adsorbents because of their high specific surface area and excellent chemical stability [9–10]. Consequently, novel carbon materials, such as graphene and its derivatives, have been largely investigated as adsorbents because graphene-based composites have good adsorption performances [11–13].

Alternatively, magnetic carbon composites have attracted more interest because they have potential application in many fields such as catalysis, sensors, and adsorption [14–16]. In the environmental remediation field, magnetic graphene oxide (GO) composites are promising adsorbents [17–21]. First, GO has rich oxygen-containing groups and a sp^2 carbon honeycomb structure, of which the former can efficiently chelate metal ions, and the latter can adsorb aromatic organics by π–π interaction. Second, magnetic characteristic makes adsorbent recycling convenient, thus overcoming the disadvantage of difficult separation of GO from the solution. To further improve the performance of the magnetic GO composites, some researchers have proposed a strategy to wrap Fe_3O_4 nanoparticles (NPs) with GO nanosheets (Fe_3O_4@GO) [22–23]. The as-prepared composites possess a core-shell structure such that the Fe_3O_4 core can prevent GO nanosheets from restacking, producing GO nanosheets perform the role of adsorbent fully.

The excellent performance of Fe_3O_4@GO has been sufficiently proven by previous research; however, firmly and completely wrapping GO nanosheets with Fe_3O_4 NPs to form an ideal core-shell structure still remains a big challenge. The Fe_3O_4@GO composites need to be synthesized stepwise, and we previously investigated some parameters affecting the structure of Fe_3O_4@GO [24]; however, the SiO_2 coating step

Corresponding authors: Zhong-liang Hu E-mail: david10103@sina.com; Zhao-hui Li E-mail: lzh69@xtu.edu.cn

was neglected. The surface modification of the SiO_2 coating is an indispensable procedure, which plays a pivotal role in forming a desired core-shell structure.

In this study, we systematically investigated the effect of a SiO_2 coating on the final structure of Fe_3O_4@GO, where Fe_3O_4 NPs were first coated by a SiO_2 layer and then wrapped by GO nanosheets (Fe_3O_4@SiO_2@GO). The adsorption capacity and regenerability of the samples were studied with various amounts of SiO_2 when Pb(II) cations were used as the adsorbate. The encapsulation effect of GOs on the regenerability of the sample was discussed. GO nanosheets were encapsulated with Fe_3O_4 NPs via covalent bonding by optimizing the SiO_2 coating and other parameters. As a result, an ideal core-shell structure was obtained with excellent regenerability. This study provides a theoretical guidance to improve the structure and performance of the Fe_3O_4@GO composites.

2. Experimental

2.1. Synthesis of the Fe_3O_4@SiO_2@GO samples

All chemicals were of analytical grade and used as received. Synthesis of the Fe_3O_4@SiO_2@GO samples included four steps: preparation of Fe_3O_4, SiO_2 coating on Fe_3O_4, surface amino-group functionalization, and an amination reaction between GO and the magnetic NPs, which was previously reported with some modification [24]. For solvothermal synthesis of Fe_3O_4, 5.0 mL of distilled water was used and the as-obtained Fe_3O_4 NPs had good dispersity and uniformity. For SiO_2 synthesis by a modified Stoker method, various amounts of tetraethyl orthosilicate (TEOS) (0, 2, 4, and 8 mL) were used to form a SiO_2 layer on the surface of Fe_3O_4. The as-prepared samples were designated as Fe_3O_4@SiO_2-1, Fe_3O_4@SiO_2-2, Fe_3O_4@SiO_2-3, and Fe_3O_4@SiO_2-4, respectively. Although Fe_3O_4 can be directly grafted by 3-aminopropyl triethoxysilane (APTES), the highly hydrophilic SiO_2 coating can react more efficiently, contributing to amelioration of the final encapsulation structure. After APTES was reacted with Fe_3O_4@SiO_2, creating a rich-NH_2 group surface, the sample (Fe_3O_4@SiO_2–NH_2) was reacted with GO, and the resulting GO-based samples were denoted as Fe_3O_4@SiO_2@GO-1, Fe_3O_4@SiO_2@GO-2, Fe_3O_4@SiO_2@GO-3, and Fe_3O_4@SiO_2@GO-4, respectively. Other optimized parameters were previously reported [24].

2.2. Characterization

The phase analysis was determined by X-ray diffractometry (XRD, D8 Advanced Diffractometer System, Bruker, Germany) with Cu-K_α radiation, and the 2θ range was from 5° to 80°. Fourier-transform infrared spectroscopy (FTIR, Spectrum One, PerkinElmer, US) was used to analyze the chemical bonding of the samples, and the data were recorded over the wavenumber range of 400–4000 cm^{-1}. Raman spectra were collected on a British Renishaw inVia confocal Raman microscope to determine the structural information. Scanning electron microscopy (SEM, JSM-6360LV, JEOL, Japan) was used to observe the morphology of the samples. Transmission electron microscopy (TEM, Tecnai G2 F20, FEI, USA) was adopted to examine the texture and morphology at an operating voltage of 200 kV. The magnetic tests were conducted on a Lakeshore 7407 vibrating sample magnetometer at room temperature.

2.3. Adsorption and regeneration experiments

Pb(II), a typical heavy metal ion, was used to act as an adsorbate for examining the adsorption of the samples. Pb(II) adsorption was performed in a shaker at 200 r/min at 25°C. 50 mg of the sample and 50 mL of the Pb(II) solution (300 $mg \cdot L^{-1}$ initial concentration) were mixed in a 100 mL conical flask and the pH was adjusted to 6. The suspension was agitated for 12 h until the adsorption equilibrium was reached. The adsorbent was then separated by an external magnet. The Pb(II) concentration in the supernatant was measured by atomic absorption spectrophotometry (AAS, ThermoFisher, iCE^{TM} 3500). The adsorption isotherm experiments were conducted under the same condition at different initial concentrations ranging from 50 to 400 $mg \cdot L^{-1}$. The adsorption capacity was calculated based on the following formula:

$$q_e = \frac{(C_0 - C_e)V}{M} \quad (1)$$

where, q_e ($mg \cdot g^{-1}$) denotes the adsorption capacity at equilibrium; C_0 and C_e ($mg \cdot L^{-1}$) signify the initial and equilibrium concentrations of Pb(II), respectively; V (L) and M (g) are the solution volume and the adsorbent mass, respectively. Adsorption–desorption experiments were performed with the same procedures. An HCl solution (0.01 M) was used as the eluent to regenerate the samples.

3. Results and discussion

3.1. SEM/TEM morphologies

The SEM morphologies of the Fe_3O_4@SiO_2 samples treated by different amounts of TEOS are presented in Fig. 1. The pristine Fe_3O_4 NPs displays a spherical morphology with good dispersity (Fig. 1(a)). After treating with 2 mL of TEOS, the Fe_3O_4 NPs were coated with a SiO_2 layer, leading to slight agglomeration (Fig. 1(b)). With increasing the TEOS amount to 4 mL, a smooth SiO_2 coating covered the surface of the magnetic NPs; however, there was some degradation to the good dispersibility of the magnetic NPs (Fig. 1(c)). However, when the TEOS amount reached 8 mL, the Fe_3O_4 NPs aggregated severely and were coated by SiO_2 to form large clusters. Additionally, some cubic SiO_2 particles were deposited on the Fe_3O_4 clusters in some places (Fig. 1(d)).

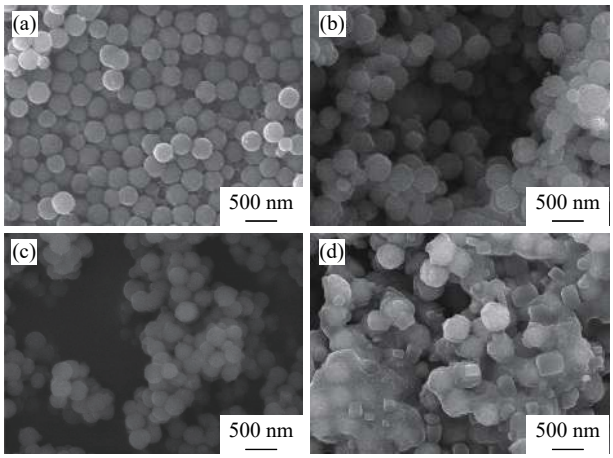

Fig. 1. SEM morphologies of (a) Fe_3O_4@SiO_2-1, (b) Fe_3O_4@SiO_2-2, (c) Fe_3O_4@SiO_2-3, and (d) Fe_3O_4@SiO_2-4.

The SEM images of the Fe_3O_4@SiO_2@GO samples prepared using different amounts of TEOS are shown in Fig. 2. Only the Fe_3O_4 NPs in Fe_3O_4@SiO_2@GO-3 were successfully wrapped by the GO nanosheets (Fig. 2(c)). In other samples, the Fe_3O_4 NPs appeared to be scattered or deposited on the GO nanosheets (Figs. 2(a), 2(b), and 2(d)). Notably, in Fe_3O_4@SiO_2@GO-1, the Fe_3O_4 NPs were loosely connected with GO, and in some places, they were nearly separated from GO nanosheets (Fig. 2(a)).

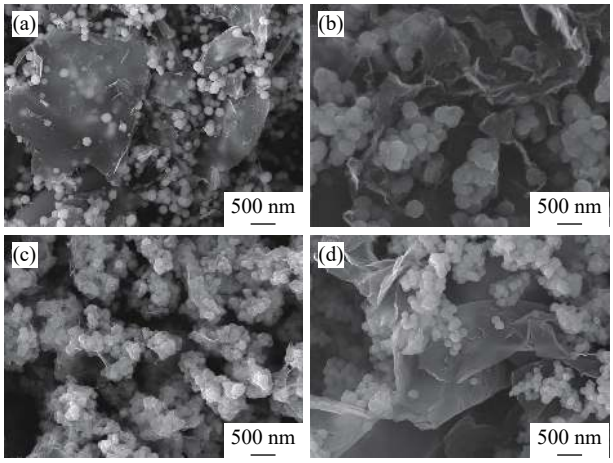

Fig. 2. SEM images of the Fe_3O_4@SiO_2@GO composites prepared using different TEOS amounts: (a) 0, (b) 2, (c) 4, and (d) 8 mL.

The SEM characterization demonstrates that the SiO_2 coating on the surface of Fe_3O_4 NPs plays a key role in deciding the structure of the final GO-based composites. A SiO_2 layer has rich hydrophilic groups on its surface [25], and these groups can effectively attract APTES to react with them. Compared with bare Fe_3O_4, the Fe_3O_4 NPs coated with a SiO_2 layer can react with APTES more easily. Additionally, $–NH_2$ groups can be uniformly and densely distributed on the entire surface of the magnetic NPs, which will be very helpful to wrap with the GO nanosheets. In Fe_3O_4@SiO_2-1, a SiO_2 layer is not coated on the Fe_3O_4 NPs; accordingly, in Fe_3O_4@SiO_2@GO-1, the encapsulation effect is the worst. For the Fe_3O_4@SiO_2-2 sample, a small amount of TEOS produces a thin or partly covered SiO_2 layer, naturally leading to a worse encapsulation effect. In the case of Fe_3O_4@SiO_2@GO-4, excess SiO_2 makes the Fe_3O_4 NPs form large clusters, which is disadvantageous to its later reactions with APTES and GO. The well-dispersed Fe_3O_4@SiO_2-3 has a smooth and uniform SiO_2 coating layer, which is a good magnetic precursor (Fig. 1(c)). Correspondingly, in Fe_3O_4@SiO_2@GO-3, the magnetic NPs are completely and strongly wrapped by GO nanosheets (Fig. 2(c)), in contrast to the other samples (Figs. 2(a), 2(b), and 2(d)).

TEM was used to further examine the morphology of the Fe_3O_4@SiO_2@GO-3 sample and its precursor (Fig. 3). A uniform layer of SiO_2 was clearly observed as a coating on the surface of Fe_3O_4 NPs for the Fe_3O_4@SiO_2-3 precursor (Fig. 3(a)). Moreover, the crumpled, silk-like GO nanosheets are firmly attached to the surface of Fe_3O_4 NPs for the Fe_3O_4@SiO_2@GO-3 sample (Fig. 3(b)).

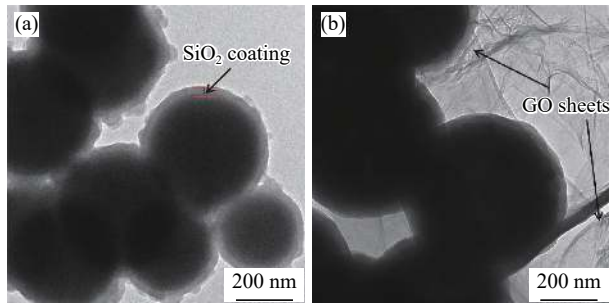

Fig. 3. TEM images of (a) Fe_3O_4@SiO_2-3 and (b) Fe_3O_4@SiO_2@GO-3.

3.2. XRD patterns

The XRD patterns of graphite oxide, Fe_3O_4, Fe_3O_4@SiO_2-3 and Fe_3O_4@SiO_2@GO-3 are shown in Fig. 4. Graphite oxide presents a peak at 2θ = ~10°, corresponding to its (001) reflection. Except for graphite oxide, the other samples have

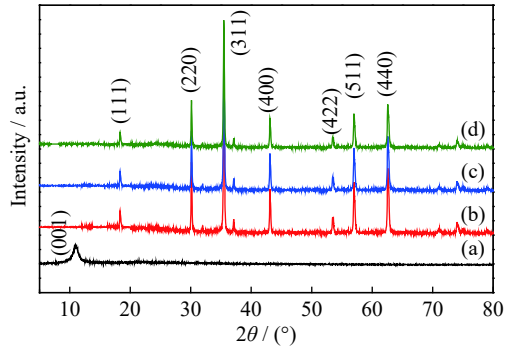

Fig. 4. XRD patterns of (a) graphite oxide, (b) Fe_3O_4, (c) Fe_3O_4@SiO_2-3, and (d) Fe_3O_4@SiO_2@GO-3.

the typical XRD patterns of magnetite (JCPDS No. 19-0629), indicating that Fe_3O_4 has been successfully prepared and its structure has been well preserved after coating a layer of SiO_2 and reacting with GO. In the Fe_3O_4@SiO_2@GO-3 sample, the XRD pattern of graphite oxide disappeared completely, inferring that its crystalline structure has been destroyed and a novel structure with wrapped nanosheets of GO was formed [26].

3.3. FTIR and Raman spectra

Fig. 5 displays the FTIR and Raman spectra of the samples. In the FTIR spectra of GO (Fig. 5(a)), the peak at 1740 cm^{-1} comes from carboxyl groups, and the peaks at ~3445 and 1610 cm^{-1} are attributed to O–H groups. The Fe_3O_4 sample has an intensive peak at ~580 cm^{-1}, which is ascribed to the stretching vibration of the Fe–O bond. For Fe_3O_4@SiO_2-3, the peaks at 1060 and 801 cm^{-1} are attributed to the asymmetric stretching vibrating of Si–O–Si and the stretching vibrating of Si–O, respectively. For Fe_3O_4@SiO_2@GO-3, the peak at 1630 cm^{-1} is attributed to the N–H groups, the peak at 1210 cm^{-1} is attributed to the C–N stretching vibrating, and the other peaks at 1065 and 580 cm^{-1} are attributed to Si–O–Si and Fe–O bonds, respectively [27–28]. The emerging new peak from the C–N bond and disappearing vibration bands are attributed to the groups of GO, indicating that amidation reaction occurs between GO and magnetic NPs, and the interaction between the magnetic NPs and GO nanosheets is covalent bonding.

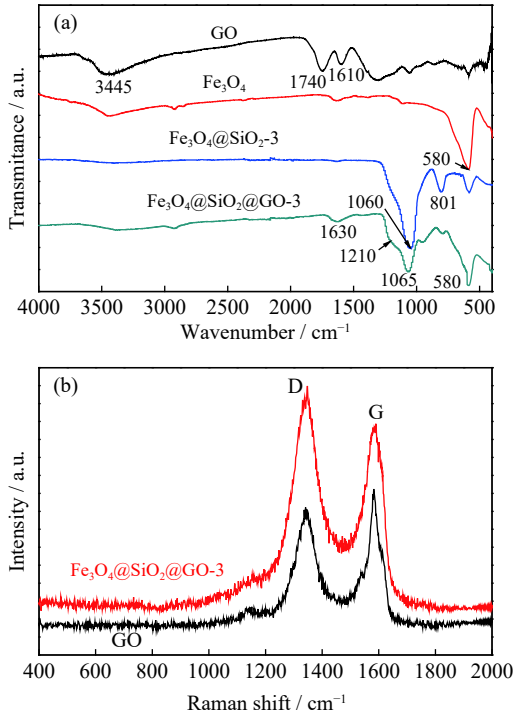

Fig. 5. (a) FTIR spectra of GO, Fe_3O_4, Fe_3O_4@SiO_2-3, and Fe_3O_4@SiO_2@GO-3; (b) Raman spectra of GO and Fe_3O_4@SiO_2@GO-3.

Raman scattering is an important tool to characterize the structure of carbonaceous materials. As shown in Fig. 5(b), both samples of GO and Fe_3O_4@SiO_2@GO-3 have a D band (~1350 cm^{-1}) and G band (~1590 cm^{-1}), which can be attributed to a disordered structure (sp^3 carbon atoms of disorders and defects) and graphite structure (sp^2 carbon atoms in graphitic nanosheets), respectively [29]. Compared with GO, the intensity ratio of D and G bands (ID/IG) of Fe_3O_4@SiO_2@GO-3 increases, indicating that GO nanosheets are more chaotically distributed in the composites, which is in agreement with the encapsulation structure of GO.

3.4. Saturation magnetization

Good magnetism is very important to promptly separate the magnetic adsorbent from solution. The saturation magnetization (*M*s) of the samples are listed in Table 1. The pure Fe_3O_4 sample has the highest saturation magnetization (75.1 $A \cdot m^2 \cdot kg^{-1}$), while the Fe_3O_4@SiO_2@GO-4 has the lowest. However, all values of the saturation magnetization are greater than 50 $A \cdot m^2 \cdot kg^{-1}$, thus all samples can be effectively separated from solution within 25 s by an external magnet, which is very beneficial to facilitate post processing.

3.5. Adsorption/regeneration performance

The isothermal adsorption of Pb(II) over Fe_3O_4@SiO_2@GO-3 is presented in Fig. 6. The Fe_3O_4@SiO_2@GO-3 sample exhibits a higher efficiency at low concentration and q_e is nearly constant at a higher C_e value (>120 $mg \cdot L^{-1}$). The related adsorption mechanism and process are elucidated by the Langmuir model [30–32], and the Langmuir isotherm equation is as follow:

$$\frac{C_e}{q_e} = \frac{C_e}{q_m} + \frac{1}{q_m K_L} \tag{2}$$

where q_m ($mg \cdot g^{-1}$) is the saturated adsorption capacity based on the complete monolayer coverage, and K_L ($L \cdot mg^{-1}$) is the Langmuir adsorption constant related to the adsorption energy.

Using the Langmuir equation, q_m and K_L are estimated to be 253 $mg \cdot g^{-1}$ and 0.073 $L \cdot mg^{-1}$, respectively. The correlation coefficient (R^2) is greater than 0.95, indicating that the adsorption process follows the Langmuir model and chemisorption dominates the adsorption mechanism.

To further investigate the performance of Fe_3O_4@SiO_2@

Table 1. Saturation magnetizations (*M*s) of samples $A \cdot m^2 \cdot kg^{-1}$

Fe_3O_4	Fe_3O_4@SiO_2@GO-1	Fe_3O_4@SiO_2@GO-2	Fe_3O_4@SiO_2@GO-3	Fe_3O_4@SiO_2@GO-4
75.1	69.5	62.8	57.1	51.3

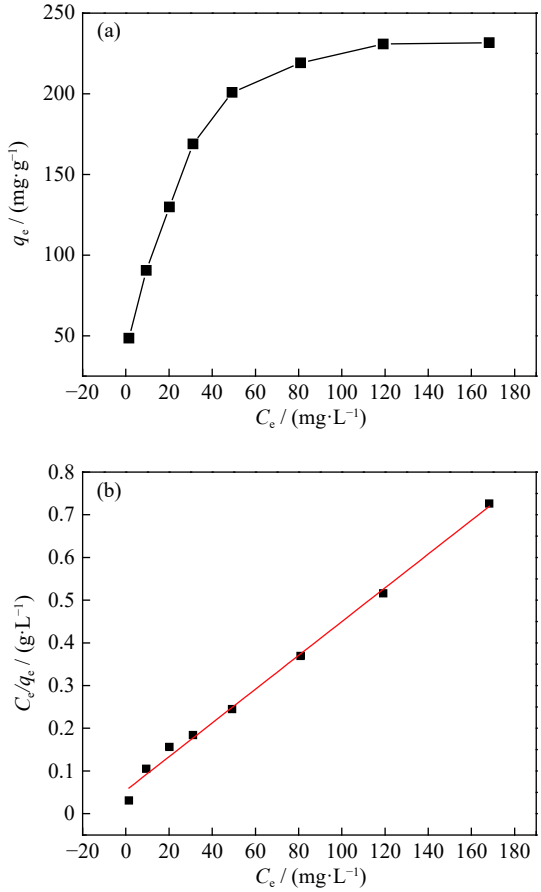

Fig. 6. (a) Pb(II) adsorption isotherm of Fe_3O_4@SiO_2@GO-3 and (b) linear fitting of adsorption isotherm plot using Langmuir model.

GO-3, Fe_3O_4@SiO_2–NH_2-3 (the sample obtained after Fe_3O_4@SiO_2-3 reacted with APTES) was tested for its Pb(II) adsorption (300 mg·L^{-1} of Pb(II) initial concentration), reaching a capacity of 173.5 mg·g^{-1}, which is ~78% the capacity of Fe_3O_4@SiO_2@GO-3. Fe_3O_4@SiO_2–NH_2-3 displays significant Pb(II) adsorption attributed to the rich-NH_2 groups on the surface that can efficiently chelate Pb(II). However, this sample tends to aggregate upon recycling, failing to act as a recyclable adsorbent.

The adsorption–desorption experiments were performed at pH of 6.0 for five cycles, and the results are presented in Fig. 7. The Fe_3O_4@SiO_2@GO-3 sample has the highest adsorption capacity and best regenerability. After five cycles, the sample can preserve ~90% of the initial adsorption capacity. However, the Fe_3O_4@SiO_2@GO-1, Fe_3O_4@SiO_2@GO-2, and Fe_3O_4@SiO_2@GO-4 samples can just maintain ~12%, ~40%, and ~20% of their initial adsorption capacities, respectively.

The performance differences between the samples are attributed to their different structures. Compared with other samples, the good performance of Fe_3O_4@SiO_2@GO-3 can be attributed to its structure. GO nanosheets are completely separated by Fe_3O_4 NPs, thus GO adsorption sites can be easily and fully accessed by adsorbates. Secondly, its structure can maintain its stability during recycling, leading to excellent regeneration. The other samples also have significant adsorption capacity; however, their regenerability deteriorates rapidly. The deposited or scattered Fe_3O_4 NPs cannot efficiently prevent re-stacking of the GO nanosheets, greatly reducing the specific surface area, and thus reducing the adsorption capacity [33].

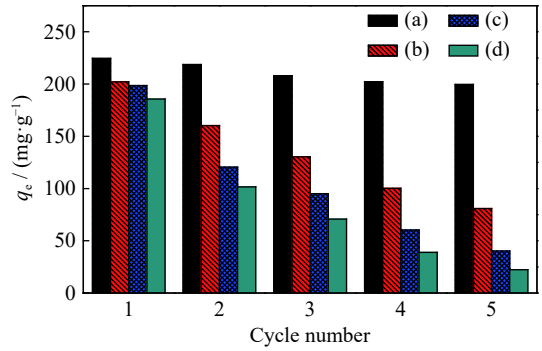

Fig. 7. Adsorption–desorption recycling of Fe_3O_4@SiO_2@GO samples toward Pb(II): (a) Fe_3O_4@SiO_2@GO-3, (b) Fe_3O_4@SiO_2@GO-2, (c) Fe_3O_4@SiO_2@GO-4, and (d) Fe_3O_4@SiO_2@GO-1.

Regenerability becomes an important property for the practical application of the GO-based adsorbents because of their relatively high cost. In contrast to the poor regenerability of the other samples, Fe_3O_4@SiO_2@GO-3 displays excellent regenerability for the following reasons. In its core-shell structure, the Fe_3O_4 NPs are completely encapsulated by GO nanosheets and the contact area between them is much larger than the other samples. Secondly, the covalent bonding is strong enough to resist the desorption environment, thus maintaining a stable structure and performance. The results in the study indicate that it can greatly enhance the regenerability of the GO-based composites by constructing an ideal core-shell structure.

4. Conclusion

Overall, the magnetic GO-based composites with a core-shell structure were prepared successfully. The Fe_3O_4 NPs are completely wrapped by the GO nanosheets and firmly tight with each other via covalent bonding. The unique structure is because of the SiO_2 layer on Fe_3O_4. An appropriate SiO_2 layer can induce GO nanosheets to react with the magnetic NPs to form GO-wrapped composites. The obtained Fe_3O_4@SiO_2@GO-3 composite has good magnetization (57.1 A·m^2·kg^{-1}) and displays a high adsorption capacity toward Pb(II). Notably, the GO-based composite possesses an excellent regenerability, maintaining ~90% adsorption capacity after five cycles. The results indicate that the regenerability of

GO-based composites can be greatly improved by designing GO-wrapped NP composites, thus guiding the synthesis of magnetic GO-based composites.

Acknowledgements

This work was financially supported by the Natural Science Foundation of Hunan Province, China (No. 2020JJ4269) and the Natural Science Foundation of China (No. 21576075).

References

[1] M.M. Khin, A.S. Nair, V.J. Babu, R. Murugan, and S. Ramakrishna, A review on nanomaterials for environmental remediation, *Energy Environ. Sci.*, 5(2012), No. 8, p. 8075.

[2] B. Kossowska, I. Dudka, R. Gancarz, and J. Antonowicz-Juchniewicz, Application of classic epidemiological studies and proteomics in research of occupational and environmental exposure to lead, cadmium and arsenic, *Int. J. Hyg. Environ. Health*, 216(2013), No. 1, p. 1.

[3] M. Laatikainen and T. Sainio, Ion exchange in complexing media – Nickel removal from ammoniacal ammonium sulfate solutions, *Chem. Eng. J.*, 373(2019), p. 831.

[4] N. Abdullah, N. Yusof, W.J. Lau, J. Jaafar, and A.F. Ismail, Recent trends of heavy metal removal from water/wastewater by membrane technologies, *J. Ind. Eng. Chem.*, 76(2019), p. 17.

[5] J.W. Lu, Z.T. Yuan, X.F. Guo, Z.Y. Tong, and L.X. Li, Magnetic separation of pentlandite from serpentine by selective magnetic coating, *Int. J. Miner. Metall. Mater.*, 26(2019), No. 1, p. 1.

[6] S. Wu, X.B. He, L.J. Wang, and K.C. Chou, High Cr(VI) adsorption capacity of rutile titania prepared by hydrolysis of $TiCl_4$ with $AlCl_3$ addition, *Int. J. Miner. Metall. Mater.*, 27(2020), No. 8, p. 1157.

[7] M.R. Awual, Assessing of lead(III) capturing from contaminated wastewater using ligand doped conjugate adsorbent, *Chem. Eng. J.*, 289(2016), p. 65.

[8] M.R. Awual and M.M. Hasan, A novel fine-tuning mesoporous adsorbent for simultaneous lead(II) detection and removal from wastewater, *Sens. Actuators B*, 202(2014), p. 395.

[9] L.F. Delgado, P. Charles, K. Glucina, and C. Morlay, The removal of endocrine disrupting compounds, pharmaceutically activated compounds and cyanobacterial toxins during drinking water preparation using activated carbon—A review, *Sci. Total Environ.*, 435-436(2012), p. 509.

[10] W.K. Buah and P.T. Williams, Granular activated carbons from palm nut shells for gold di-cyanide adsorption, *Int. J. Miner. Metall. Mater.*, 20(2013), No. 2, p. 172.

[11] M.F. Li, Y.G. Liu, G.M. Zeng, N. Liu, and S.B. Liu, Graphene and graphene-based nanocomposites used for antibiotics removal in water treatment: A review, *Chemosphere*, 226(2019), p. 360.

[12] X. Liu, X.T. Xu, J. Sun, A. Alsaedi, T. Hayat, J.X. Li, and X.K. Wang, Insight into the impact of interaction between attapulgite and graphene oxide on the adsorption of U(VI), *Chem. Eng. J.*, 343(2018), p. 217.

[13] X.T. Liu, K. Pang, H. Yang, and X.Z. Guo, Intrinsically microstructured graphene aerogel exhibiting excellent mechanical performance and super-high adsorption capacity, *Carbon*, 161(2020), p. 146.

[14] R. Zhang, N. Lu, J.X. Zhang, R.H. Yan, J. Li, L.H. Wang, N. Wang, M. Lv, and M. Zhang, Ultrasensitive aptamer-based protein assays based on one-dimensional core-shell nanozymes, *Biosens. Bioelectron.*, 150(2020), art. No. 111881.

[15] M. Zhang, L. Ding, J. Zheng, L.B. Liu, H. Alsulami, M.A. Kutbi, and J.L. Xu, Surface modification of carbon fibers with hydrophilic Fe_3O_4 nanoparticles for nickel-based multifunctional composites, *Appl. Surf. Sci.*, 509(2020), art. No. 145348.

[16] Y. Ling, M. Zhang, J. Zheng, J.L. Xu, T. Hayat, and N.S. Alharbi, Formation of uniform magnetic C@CoNi alloy hollow hybrid composites with excellent performance for catalysis and protein adsorption, *Dalton Trans.*, 47(2018), No. 23, p. 7839.

[17] V. Chandra, J. Park, Y. Chun, J.W. Lee, I.C. Hwang, and K.S. Kim, Water-dispersible magnetite-reduced graphene oxide composites for arsenic removal, *ACS Nano*, 4(2010), No. 7, p. 3979.

[18] Y.X. Ma, W.J. Shao, W. Sun, Y.L. Kou, X. Li, and H.P. Yang, One-step fabrication of β-cyclodextrin modified magnetic graphene oxide nanohybrids for adsorption of Pb(II), Cu(II) and methylene blue in aqueous solutions, *Appl. Surf. Sci.*, 459(2018), p. 544.

[19] M.S. Raghu, K.Y. Kumar, M.K. Prashanth, B.P. Prasanna, R. Vinuth, and C.B.P. Kumar, Adsorption and antimicrobial studies of chemically bonded magnetic graphene oxide–Fe_3O_4 nanocomposite for water purification, *J. Water Process Eng.*, 17(2017), p. 22.

[20] J.H. Miao, F.H. Wang, Y.J. Chen, Y.Z. Zhu, Y. Zhou, and S.T. Zhang, The adsorption performance of tetracyclines on magnetic graphene oxide: A novel antibiotics absorbent, *Appl. Surf. Sci.*, 475(2019), p. 549.

[21] S.C. Chang, Q. Zhang, Y.K. Lu, S.Z. Wu, and W. Wang, High-efficiency and selective adsorption of organic pollutants by magnetic $CoFe_2O_4$/graphene oxide adsorbents: Experimental and molecular dynamics simulation study, *Sep. Purif. Technol.*, 238(2020), art. No. 116400.

[22] H. Wei, W.S. Yang, Q. Xi, and X. Chen, Preparation of Fe_3O_4@graphene oxide core-shell magnetic particles for use in protein adsorption, *Mater. Lett.*, 82(2012), p. 224.

[23] S.D. Pan, X.H. Chen, H.Y. Shen, X.P. Li, M.Q. Cai, Y.G. Zhao, and M.C. Jin, Rapid and effective sample cleanup based on graphene oxide-encapsulated core-shell magnetic microspheres for determination of fifteen trace environmental phenols in seafood by liquid chromatography-tandem mass spectrometry, *Anal. Chim. Acta*, 919(2016), p. 34.

[24] Z.L. Hu, S.L. Qin, Z. Huang, Y.R. Zhu, L.J. Xi, and Z.H. Li, Stepwise synthesis of graphene oxide-wrapped magnetic composite and its application for the removal of Pb(II), *Arab. J. Sci. Eng.*, 42(2017), No. 10, p. 4239.

[25] S.W. Yang, J.C. Liu, F. Pan, X.Z. Yin, L.X. Wang, D.Z. Chen, Y.S. Zhou, C.X. Xiong, and H. Wang, Fabrication of self-healing and hydrophilic coatings from liquid-like graphene@SiO_2 hybrids, *Compos. Sci. Technol.*, 136(2016), p. 133.

[26] Z.L. Hu, X.J. Zhang, J.Y. Li, and Y.R. Zhu, Comparative study on the regeneration of Fe_3O_4@graphene oxide composites, *Front. Chem.*, 8(2020), art. No. 150.

[27] S.K. Singh, M.K. Singh, P.P. Kulkarni, V.K. Sonkar, J.J.A. Grácio, and D. Dash, Amine-modified graphene: Thrombo-protective safer alternative to graphene oxide for biomedical applications, *ACS Nano*, 6(2012), No. 3, p. 2731.

[28] R.H. Gangupomu, M.L. Sattler, and D. Ramirez, Comparative study of carbon nanotubes and granular activated carbon: Physicochemical properties and adsorption capacities, *J. Hazard. Mater.*, 302(2016), p. 362.

[29] S. Alwarappan, A. Erdem, C. Liu, and C.Z. Li, Probing the electrochemical properties of graphene nanosheets for biosensing applications, *J. Phys. Chem. C*, 113(2009), No. 20, p. 8853.

[30] M. Zhang, Y. Ling, L.B. Liu, J.L. Xu, J.X. Li, and Q.L. Fang, Carbon supported PdNi alloy nanoparticles on SiO_2 nanocages with enhanced catalytic performance, *Inorg. Chem. Front.*, 7(2020), No. 17, p. 3081.

[31] S.A. Singh, B. Vemparala, and G. Madras, Adsorption kinetics of dyes and their mixtures with Co_3O_4–ZrO_2 composites, *J. Environ. Chem. Eng.*, 3(2015), No. 4, p. 2684.

[32] J. Zheng, M. Zhang, T. Miao, J.X. Yang, J.L. Xu, N.S. Alharbi, and M. Wakeel, Anchoring nickel nanoparticles on three-dimensionally macro-/mesoporous titanium dioxide with a carbon layer from polydopamine using polymethylmethacrylate microspheres as sacrificial templates, *Mater. Chem. Front.*, 3(2019), No. 2, p. 224.

[33] A.B. Bourlinos, D. Gournis, D. Petridis, T. Szabó, A. Szeri, and I. Dékány, Graphite oxide: Chemical reduction to graphite and surface modification with primary aliphatic amines and amino acids, *Langmuir*, 19(2003), No. 15, p. 6050.